PAPER

Self-templating synthesis of nitrogen-decorated hierarchical porous carbon from shrimp shell for supercapacitors

Feng Gao,[ab] Jiangying Qu,*[ab] Chuang Geng,[a] Guanghua Shao[a] and Mingbo Wu*[c]

Nitrogen-doped hierarchical porous carbon (HPC) was prepared from shrimp shell using its intrinsic mineral scaffold ($CaCO_3$) as the self-template combined with KOH activation. The roles of the template removal and KOH activation on the hierarchical porous structure of the obtained HPC were discussed in detail. The as-made HPC with abundant micropores, mesopores and interconnected macropores exhibits high electrochemical performance when used as the supercapacitor electrode. The specific surface area of HPC can be easily controlled *via* changing the activation temperature, and the natural nitrogen in shrimp shell can be preserved, which favor the final electrochemical property. Attributing to the synergetic electrochemical activity of the accessible porosity and the heteroatom, the hierarchical porous carbon pyrolyzed at 700 °C displays the largest specific capacitance of 348 F g^{-1} in a 6 M KOH electrolyte. The hierarchical porosity of the obtained carbon provides a well-defined ion pathway and electrolyte reservoir, allowing for rapid ionic transportation. This self-templating method represents a very attractive approach for the scalable production of hierarchical porous carbons from natural biomass containing both nitrogen/carbon sources and intrinsic templates.

Introduction

Electrochemical capacitors (ECs), also known as super-capacitors, capitalize on the high efficiency and performance stability of fast electrosorption of electrolyte ions at the charged interface.[1–3] As an effective electrode, porous carbon materials have a high capacitance, which is mainly dependent on their surface properties and porous structures. Various carbons including ultramicroporous, microporous, and mesoporous carbon with narrow pore size distribution have been widely applied to the electrode materials of ECs.[4–8] However, their pore textures are not suitable for high-rate supercapacitors due to the poor ion transport in inner pores. Hence, novel porous carbon with hierarchical porosity, namely, macropores combined with micropores and mesopores, is highly desired due to its unique structural features in comparison to conventional micro- and/or mesoporous materials with uniform pore dimensions. Xia *et al.* reported that the carbon with a hierarchical porous structure showed excellent electrochemical behavior with a specific gravimetric capacitance of 223 F g^{-1} and a 73% retained ratio.[9]

As a promising material for energy storage, hierarchical porous carbon (HPC) with well-defined pore dimensions and topologies offers minimized diffusive resistance to mass transport due to its macropores and high surface area for active site dispersion over that of the micro- and/or mesopores.

Lots of extraordinary studies described the synthesis of HPC *via* hard-templating, soft-templating, dual-templating, or non-templating strategies. The most commonly used technique for the fabrication of HPC is the hard-templating method with hierarchically nanostructured silica, MOF or diatomite as the template to impregnate with an appropriate carbon source, followed by the carbonization of the composites, and subsequent removal of the template.[10–14] For example, Hu *et al.* reported that the macroscopic carbon monoliths with both mesopores and macropores were successfully prepared by using meso-/macroporous silica as the template and a mesophase pitch as the precursor.[10] Generally, hard-template methods suffer from drawbacks such as complicated structures of the template, the massive use of the template and tedious template removal processes. Alternatively, HPC was also synthesized from novel benzoxazine chemistry using a soft-templating method and KOH chemical activation.[15] Furthermore, a modified dual-templating strategy for the architectural design of 3D HPC as a promising electrode material for high-rate ECs was developed by using polystyrene and Pluronic F127 as macro- and mesoporous templates, respectively.[16] Those methods still involve the massive use of soft templates and organic solvents, and the experimental conditions universally need to be very

[a]*Faculty of Chemistry and Chemical Engineering, Liaoning Normal University, Dalian, Liaoning, 116029, China. E-mail: qujy@lnnu.edu.cn; Tel: +86-411-82158329*

[b]*Carbon Research Laboratory, Center for Nano Materials and Science, School of Chemical Engineering, State Key Lab of Fine Chemicals, Dalian University of Technology, Dalian, 116024, China*

[c]*State Key Laboratory of Heavy Oil Processing, China University of Petroleum, Qingdao, 266580, China. E-mail: wumb@upc.edu.cn; Tel: +86-532-86983452*

This journal is © The Royal Society of Chemistry 2016

J. Mater. Chem. A, 2016, **4**, 7445–7452 | 7445

precise at low carbon precursor concentration, which hinders the mass production.[17] In the non-templating route, the process involves the activation of a carbon precursor with H_3PO_4 followed by activation of KOH, and the resulting carbon exhibited a specific capacitance of 306 F g^{-1} in an aqueous electrolyte.[18] However, the currently effective template methods and acid/base activation strategies suffer from the drawbacks of either high cost or tedious steps. Therefore, the sustainable and scalable methods for the production of HPCs are still in great demand.

Besides improving the wettability and increasing the charge screening ability of carbon, nitrogen-sites at the carbon surface can facilitate charge transfer across the electrode/electrolyte interface. Such redox-sites may contribute significantly to the energy storage by enabling access to reversible faradaic reactions and possibly pseudocapacitance.[19–22] As nitrogen-doped carbon exhibits improved performance, some techniques have been focused on the introduction of nitrogen species into the carbon framework, which is achieved either by post-treatment of carbon with nitrogen-containing precursors (*e.g.* melamine and polyvinylpyridine) or *via* treating carbon materials with ammonia gas.[23] One ideal choice is preparing nitrogen-doped carbon from natural biomass, which acts both as nitrogen and carbon sources.

As an important marine organism, around 1.3 million tons of shrimp are produced in China each year. Shrimp shell, a kind of food waste in high quantity, is a cheap and reliable biomass source without increasing competition for food. Shrimp shell is composed of naturally inorganic $CaCO_3$ (about 60%) along with a nitrogen-containing polysaccharide named as chitin. The former can act as the natural template for the synthesis of porous carbon, meanwhile, the latter may be a good precursor for the fabrication of nitrogen-doped porous carbon. White *et al.* reported that prawn shell was used to make mesoporous carbon with its intrinsic mineral scaffold as the template.[24] However, to our knowledge, the fabrication of hierarchical porous carbon has been rarely reported.

In this study, HPC was fabricated from waste shrimp shell by the self-templating route combined with KOH activation and subsequent $CaCO_3$ removal. It is found that KOH activation can create the micropores in the carbon skeleton, while the removal of the $CaCO_3$ template that naturally exists in shrimp shell causes mesopores and macropores. The porosity of HPC could be easily controlled by adjusting the pyrolysis temperature under a fixed weight ratio of shrimp shell to KOH. The HPC-based supercapacitor demonstrates good electrochemical performance with a large specific capacitance, high power density, and long cyclic stability.

Experimental

Synthesis of nitrogen-decorated HPCs from shrimp shell

Bohai shrimp shell was used as the raw material in this study. Shrimp shell and KOH with a mass ratio of 1 : 4 were thoroughly mixed together and dried at 80 °C overnight. Then the dried mixture was pyrolyzed at 600–800 °C for 1 h in a horizontal furnace in an Ar atmosphere. Then, the obtained sample was

sufficiently dissolved in acetic acid at room temperature until the complete removal of $CaCO_3$. Finally, the samples were thoroughly washed with deionized water until the solution became neutral. After exposure in an oven at 80 °C, a series of samples were harvested and denoted as C/KOH-*T* (*T* = 600, 700 or 800 °C). For comparison, shrimp shell was pyrolyzed at 700 °C for 1 h in the absence of KOH to yield the C-700 sample. Furthermore, C–$CaCO_3$/KOH-700 was produced *via* $CaCO_3$ removal and subsequent KOH activation.

Electrochemical measurements

The electrochemical performance of the as-obtained samples was investigated using a three-electrode cell and a two-electrode cell at room temperature. The working electrodes were fabricated by mixing the prepared powder with 10 wt% acetylene black and 5 wt% polytetrafluoroethylene (PTFE) binder. A small amount of ethanol was added to the mixture to produce a homogeneous paste. The mixture was pressed onto nickel foam current-collectors (1.5 cm in diameter) to make electrodes. The mass of the active material was in a range of 4–5 mg per electrode. Before the electrochemical test, the as-prepared electrode was soaked overnight in a 6 M KOH electrolyte. For the three-electrode cell, platinum foil and an Hg/HgO electrode were used as the counter and reference electrodes, respectively. For the two-electrode cell, two symmetrical work electrodes were assembled and tested at different cell voltages. The cyclic voltammetry (CV) measurement was conducted on a CHI660D electrochemical workstation (Shanghai Chenhua) and the galvanostatic charge–discharge measurement was performed on a Land CT2001A cycler (Wuhan Land Instrument Company, China) at room temperature. The electrical conductivity of as-made carbons was measured by a two-probe method. *I–V* curves were recorded with a CHI 660E electrochemical workstation. The morphologies and structures of the as-obtained products were examined using field emission scanning electron microscopy (SEM, Hitachi Ltd SU8010), X-ray photoelectron spectroscopy (XPS, Thermo VG Scientific Sigma Probe Spectrometer) and elemental analysis (Elemental Analyzer Vario EL III). The Brunauer–Emmett–Teller (BET) surface area of as-synthesized samples was determined by physisorption of N_2 at 77 K using a Micromeritics ASAP 2020 analyzer.

Results and discussion

Fig. 1 illustrates the strategy for the self-templating synthesis of nitrogen-decorated HPC with hierarchical pores using shrimp shell as the carbon precursor with the assistance of KOH activation. It is well known that KOH activation is a widely used method to produce micropores of carbon materials, in which two main mechanisms are involved according to a previous report.[25] As shrimp shell is concerned, aromatization occurs at increasing heat treatment temperature to gradually develop the basic structural unit of a graphitic structure below 700 °C, then the graphite layers expand by rapidly removing intercalated potassium above 700 °C.[25] In this case, shrimp shell was firstly activated by KOH in an Ar atmosphere for producing

7446 | *J. Mater. Chem. A*, 2016, **4**, 7445–7452

This journal is © The Royal Society of Chemistry 2016
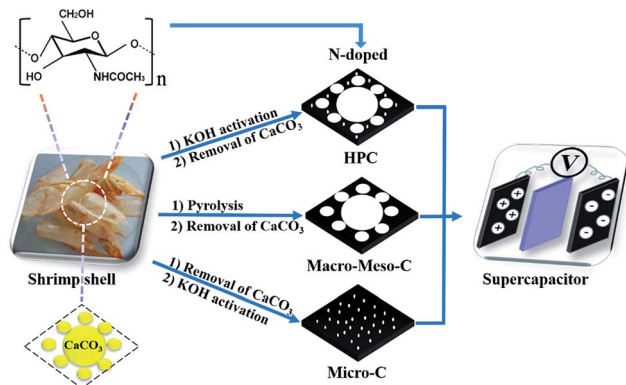
Fig. 1 Synthesis schematic of HPC, macro–meso-C and micro-C from shrimp shell.

micropores at 600–800 °C, then the intrinsic $CaCO_3$ template was removed by acetic acid to fabricate the macropores and mesopores in the resultant carbon. HPC with hierarchical porosity was obtained and used as the electrode material for ECs. The above-mentioned self-templating method for tailoring of the pore sizes of the resultant carbons is different from those of other hard- or soft-template methods, in which an additional template is needed.[10–14]

Fig. 2 shows the representative SEM images of raw shrimp shell and the C/KOH-700 sample with different magnifications. Shrimp shell is composed of lamellar layers (Fig. 2a), on which lots of particles are densely aggregated on their surfaces (Fig. 2b). Such layer structures play an important role on the final shape of the obtained product. As expected, flat microplates for the C/KOH-700 sample with a rough surface are observed (Fig. 2c and d), on which disordered macropores are present on the surfaces of the layer architectures (Fig. 2e). These structures significantly increase the charge storage and capacitance of the samples.[26,27] The presence of macropores further supports the fact that $CaCO_3$ in shrimp shell acts as the template, which enables the easy control of the porous structures of the obtained HPC.

The porosity of the obtained samples was further investigated using nitrogen adsorption–desorption measurements (Fig. 3a). The pore size distributions of all samples in the range
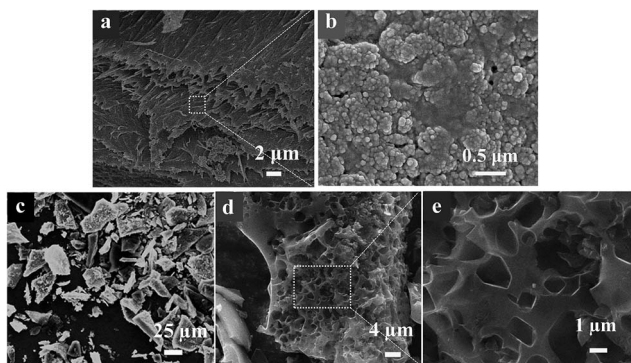

Fig. 2 SEM images of (a and b) raw shrimp shell and (c–e) C/KOH-700 sample with different magnifications.
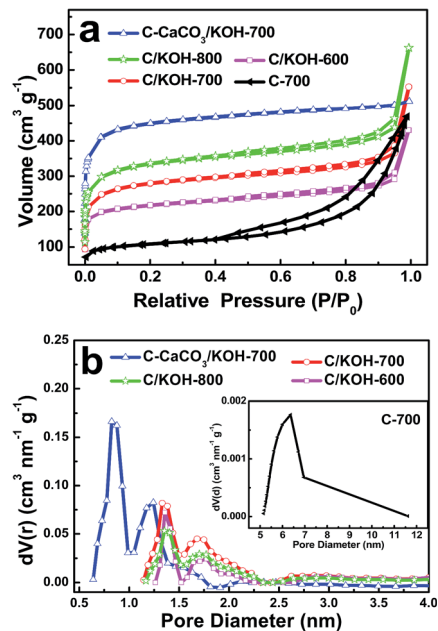

Fig. 3 (a) Nitrogen adsorption and desorption isotherms and (b) corresponding pore size distributions of C-700, C/KOH-600, C/KOH-700, C/KOH-800 and C–CaCO₃/KOH-700 samples.

of a micropore and mesopore are summarized in Fig. 3b. For the C-700 sample, its isotherm belongs to the type IV sorption isotherm with a large H3 hysteresis loop at $P/P_0 = 0.4$–0.8 and a further uptake of N_2 in the high relative pressure region at $P/P_0 = 0.9$–1.0, reflecting a substantial existence of massive mesopores and macropores. The mesoporous size of C-700 is centered at 6.5 nm (the inset of Fig. 3b), which is mainly attributed to the presence of intrinsic $CaCO_3$ in the shrimp shell. For the C–CaCO₃/KOH-700 sample, which was activated by KOH after the removal of $CaCO_3$, shows a characteristic of type I sorption isotherm at $P/P_0 = 0.01$–0.1, indicating that the micropore is dominant. The primary and secondary micropore sizes of C–CaCO₃/KOH-700 are centered at 0.8 and 1.2 nm, respectively. Such a result demonstrates that KOH activation can only create the micropores in the carbon skeleton, which is in accordance with the reference reports.[4,28] On the basis of these results, we can deduct that direct pyrolysis of shrimp shell with KOH can produce hierarchical pores in the resultant carbons. As expected, C/KOH-600, C/KOH-700, and C/KOH-800 samples display a combined type IV/I sorption isotherm, indicating the presence of mesopores and micropores.[29] In conjunction with the pore size data shown in Fig. 3b, these results indicate the presence of two distinct miocropore size distributions for all the above-mentioned samples denoted as primary micropores (1.4 nm) and secondary micropores (1.8 nm), as well as a large range of mesopore distribution (2.0–4.0 nm). It is obvious that the mesopore sizes of C-700, C/KOH-700 and C–CaCO₃/KOH-700 are significantly reduced, indicating the importance of the sequence of the removal of intrinsic $CaCO_3$ in shrimp shell for tuning the pore sizes of the obtained carbons. Furthermore, an additional uptake in the high relative pressure region ($P/P_0 = 0.9$–1.0) is also observed in

This journal is © The Royal Society of Chemistry 2016

J. Mater. Chem. A, 2016, 4, 7445–7452 | 7447

C/KOH-600, C/KOH-700, and C/KOH-800 samples. This indicates typical existence of macropores, as observed in the SEM image of C/KOH-700. The nitrogen adsorption–desorption measurements indicate that the intrinsic $CaCO_3$ of shrimp shell can be used as the self-template to produce mesopores and macropores, and KOH activation can help to create micropores in the final carbons.

Detailed information on the BET surface area (S_{BET}) is also summarized in Table 1. The C-700 sample shows a low S_{BET} of 315 m^2 g^{-1} and a small volume of 0.65 cm^3 g^{-1}. Significant increases are observed in both surface area and pore volume for C/KOH-600, C/KOH-700, and C/KOH-800 samples as the activation temperature increases from 600 to 800 °C. S_{BET} reaches 1087, 1113, and 1343 m^2 g^{-1} as well as the pore volume runs up to 0.60, 0.68, and 0.73 cm^3 g^{-1} for C/KOH-600, C/KOH-700 and C/KOH-800 samples, respectively. Such changes of S_{BET} depend on the pyrolysis temperature, *i.e.*, the higher the temperature, the larger the S_{BET} of the resultant carbons. The S_{BET} of C–CaCO$_3$/KOH-700 (2032 m^2 g^{-1}) is much larger than that of HPC due to the more micropores developed in it. Furthermore, all of the as-made carbons except C-700 have the larger S_{mic} than S_{mes}. The above-mentioned results indicate that KOH plays an important role in the creation of microporous structures and improvement of the specific surface area in the final product.[4,28]

In order to elucidate the surface composition of the porous carbons and their role in the electrochemical performance of the obtained HPCs, the incorporated nitrogen of the carbon network was further analyzed by XPS (Fig. 4). From the XPS spectra of N 1s (Fig. 4b), the most pronounced peaks represent pyridinic N (N-6 at 398.2 eV), pyrrolic/pyridonic N (N-5 at 399.8 eV), quaternary N (N–Q at 400.5 eV) and oxidized N (N–X at 402.0 eV).[30,31] For comparison, the quantitative analyses of the carbon samples are listed in Table 2. Nitrogen content decreases significantly with the temperature increasing from 600 to 800 °C during KOH activation, while the carbon content follows in the reverse order. The amount of N-5 species is significantly high in all samples with the content in the range of 47.2–71.4%, whereas N–X species only account for a small part of the nitrogen species. It is reported that the N-5 form with planar structures and good electrical conductivity are generally found to be more active than the N–X form with 3D structures in a supercapacitor.[32,33] The obvious peaks for C 1s peaks represent C═C (at 284.6 eV) and C–C (at 285.5 eV) with the total content
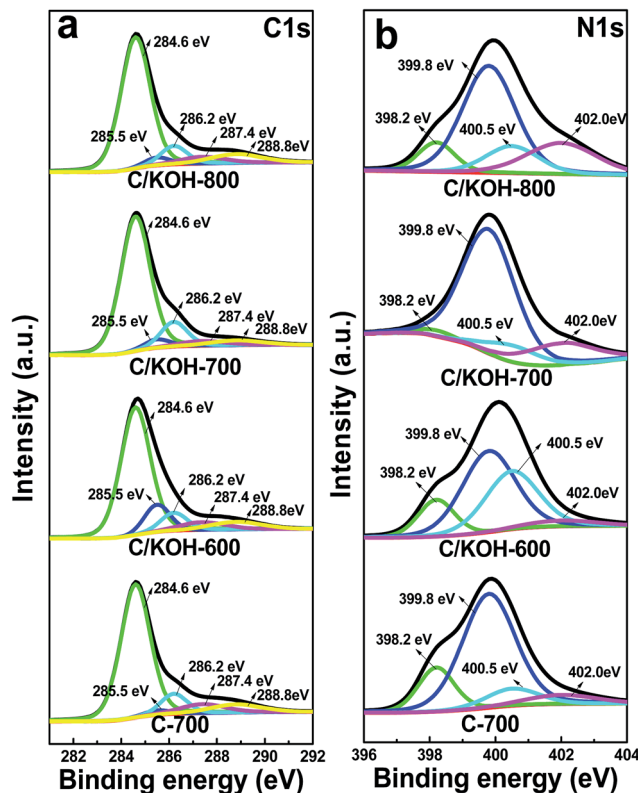

Fig. 4 XPS spectra of deconvoluted high-resolution (a) C 1s and (b) N 1s for C/KOH-800, C/KOH-700, C/KOH-600 and C-700 samples.

above 75% (Fig. 4a), indicating the formation of a carbon skeleton after the pyrolysis of shrimp shell.[34]

The electrochemical performance of the shrimp shell-derived carbons for supercapacitors was performed in a 6 M KOH electrolyte using three-electrode cells. Fig. 5a shows CV curves of the obtained carbons at a scan rate of 5 mV s^{-1}. C-700, C/KOH-600, C/KOH-700, C/KOH-800 and C–CaCO$_3$/KOH-700 all show good rectangular-like shapes. It is clear that the samples activated by KOH exhibit larger rectangular-like shapes than that of C-700. And the capacitance decreases in the following order at 5 mV s^{-1}: C/KOH-700 > C–CaCO$_3$/KOH-700 > C/KOH-600 > C/KOH-800 > C-700. Such obvious differences in the CV curves are related to their different porous structures and nitrogen-doping content. The galvanostatic charge/discharge curves at a current density of 50 mA g^{-1} are used to characterize

Table 1 Porous properties of the carbons derived from shrimp shell

Sample	S_{BET}^{a} (m^2 g^{-1})	S_{mic}^{b} (m^2 g^{-1})	S_{mes}^{c} (m^2 g^{-1})	V_{total}^{d} (cm^3 g^{-1})	Pore size (nm)
C-700	315	129	186	0.65	5.10–6.95
C/KOH-600	1087	801	286	0.60	1.26–2.35
C/KOH-700	1113	889	224	0.68	1.13–2.35
C/KOH-800	1343	1039	304	0.73	1.15–2.35
C–CaCO$_3$/KOH-700	2032	1735	297	0.83	0.64–1.83

^{a} S_{BET} is the specific surface area obtained by the BET method. ^{b} S_{mic} is the microporous surface area calculated by the *t*-plot method. ^{c} S_{mes} is the mesoporous surface area by the *t*-method external surface area ($S_{mes} = S_{BET} - S_{mic}$). ^{d} V_{total} is the total volume calculated at a relative pressure of 0.99.

Table 2 The contents of C, N and O in HPCs from elemental analysis and XPS analyses

Sample	Elemental analysis (wt%)			C-1 [%] 284.6 eV	C-2 [%] 285.5 eV	N-6 [%] 398.2 eV	N-5 [%] 399.8 eV	N–Q [%] 400.5 eV	N–X [%] 402.0 eV
	C	N	O						
C-700	60.6	3.7	33.8	72.9	2.2	17.5	65.8	9.9	6.8
C/KOH-600	61.6	7.5	28.2	68.1	11.5	14.6	47.2	33.8	4.4
C/KOH-700	68.5	3.6	25.9	75.0	4.1	2.4	71.4	9.6	16.6
C/KOH-800	81.3	2.1	16.0	72.8	3.8	10.4	54.8	13.9	20.9
C–CaCO$_3$/KOH-700	67.7	3.6	26.7	—	—	—	—	—	—

the capacitive properties of the carbons, as shown in Fig. 5b. Such results agree with the description of CV curves. Fig. 5c gives the relationships between the specific capacitance (C_s) and the current density according to the galvanostatic charge and discharge results. The value of C_s is calculated according to $C_s = I \times \Delta t/(\Delta V \times m)$ from the discharge curves, where I is the constant discharge current, Δt is the discharge time, ΔV is the potential drop during discharge time, and m is the total mass of the active electrode materials.[35] The C/KOH-700 electrode shows 348 F g^{-1} at the current density of 50 mA g^{-1}, which is lower than 362 F g^{-1} of the C–CaCO$_3$/KOH-700 electrode in the same current density. In contrast, good capacitance retention is observed in the C/KOH-700 supercapacitor in comparison to that of C–CaCO$_3$/KOH-700 in the tested range of the current density above 100 mA g^{-1}. In this case, the charge storage capacities of the obtained samples decrease in the following order: C/KOH-700 > C–CaCO$_3$/KOH-700 > C/KOH-600 > C/KOH-800 > C-700. Such performances are attributed to the character of the porous structures, the nitrogen content as well as the type of N-configuration of the samples. Among all samples mentioned above, C/KOH-700 presents the highest

performance for 348, 328, 320, 300, 295 and 290 F g^{-1} at the current density of 0.05, 0.1, 0.2, 0.5, 1.0 and 2.0 A g^{-1}, respectively. These values are significantly higher than those of previously reported N-doped hydrothermal carbons (300 F g^{-1} at 0.1 A g^{-1}),[36] activated carbon (250 F g^{-1} at 0.05 A g^{-1}),[27] mesoporous N-rich carbon (305 F g^{-1} at 0.2 A g^{-1}),[37] and N, P, and O co-doped carbon (260 F g^{-1} at 0.05 A g^{-1}).[33] According to previous reports, the pore sizes of the samples are the most effective factor in a double-layer formation, and nitrogen functionalities play important roles in improving the surface wettability and capacitance.[27,31,38,39] C-700, with the lowest S_{BET} of 315 m^2 g^{-1} and the moderate nitrogen content (3.7 wt%), exhibits the lowest electrochemical capacitance among all samples. It is observed that the increased specific surface area can help to get the high charge storage capacity. Although the C/KOH-600 sample has a much lower specific surface area (1087 m^2 g^{-1}) than 1343 m^2 g^{-1} of the C/KOH-800 sample, it has a larger capacitance, which is contributed to the induced pseudocapacitance brought by its N-rich functionalities (7.5 wt%). On the other hand, both C/KOH-700 and C–CaCO$_3$/KOH-700 samples contain the similar nitrogen content, but the
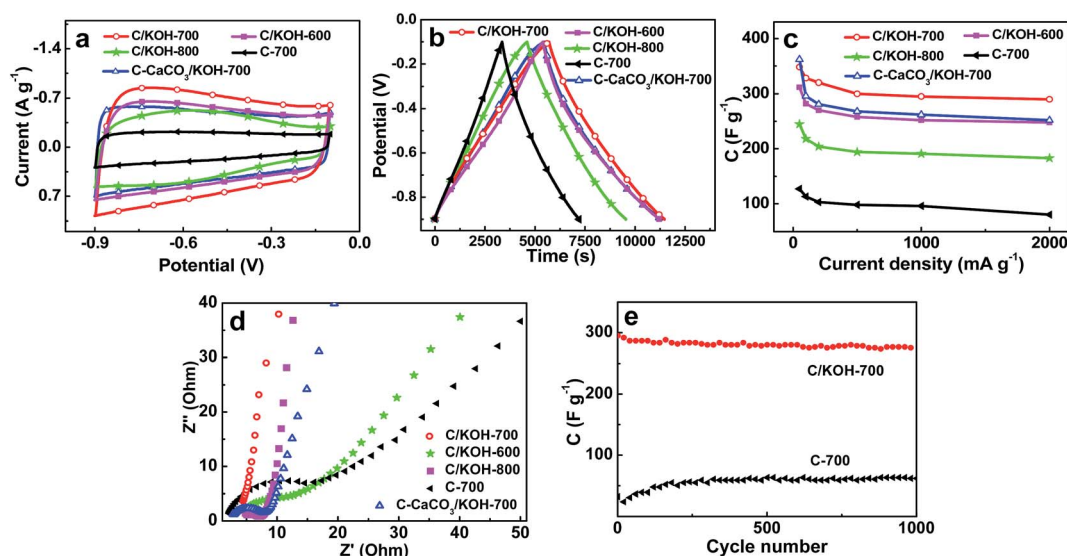

Fig. 5 Electrochemical performances of C-700, C/KOH-600, C/KOH-700, C/KOH-800 and C–CaCO$_3$/KOH-700 samples measured in a three-electrode system in a 6 M KOH electrolyte: (a) CV cures at the scan rate of 5 mV s^{-1}; (b) charge–discharge curves at the current density of 100 mA g^{-1}; (c) specific capacitances of carbon samples at different current densities; (d) Nyquist plots of various carbon samples; (e) cycling performances of C/KOH-700 and C-700 samples for 1000 cycles loaded at a current density of 1 A g^{-1}.

former exhibits higher performance than the latter due to their different pore sizes. The hierarchical pore structure of C/KOH-700 provides a well-defined ion pathway and electrolyte reservoir, allowing for rapid ionic motion.[9,28,40,41] However, ion transport in the C–CaCO$_3$/KOH-700 sample might be hindered by its narrow micropore size under high current density, though C–CaCO$_3$/KOH-700 has a much higher specific surface area (2032 m^2 g^{-1}) than 1113 m^2 g^{-1} of C/KOH-700.

Nyquist plots of the carbons in Fig. 5d provide complementary information to further understand their capacitive behaviors. It is reported that a larger diameter of the semicircle for the electrode reflects the existence of higher R_{ct} (charge-transfer resistance) in the high frequency region, indicating the rich nitrogen-containing functional groups in the samples.[42] It is observed that the R_{ct} of the as-made samples is in the following order: C/KOH-700 < C/KOH-800 < C–CaCO$_3$/KOH-700 < C-700 < C/KOH-600, indicating an increasing trend of R_{ct}. The electrical conductivity of the obtained carbons was measured by a two-probe method. The conductivity of C–CaCO$_3$/KOH-700 and C-700 are 140 and 31 S m^{-1}, while the conductivity of C/KOH-600, C/KOH-700 and C/KOH-800 are 22, 156 and 150 S m^{-1}, respectively. Such results are in line with the synergetic effects of the increased nitrogen content as well as high surface area and large pore size in the resultant carbons. Among them, C/KOH-700 with the moderate nitrogen content and surface area exhibits the highest conductivity. The stability of the capacitance performance of C/KOH-700 and C-700 samples was evaluated by 1000 cycles at a current density of 1 A g^{-1} (Fig. 5e). The C_s of the C-700 electrode is found to gradually increase in the first 150 cycles, which might contribute to the increasing surface wettability. During the rest of the cycles, the C_s of C-700

is relatively stable about 60 F g^{-1}, while that of the C/KOH-700 electrode slightly drops 6.4% from 295 to 276 F g^{-1}, demonstrating the superior long-term stability of the electrode material. Such improved stability and high capacitance can be related to its hierarchical porous structure which provides a well-defined ion pathway and electrolyte reservoir.

The capacitive behaviors of C/KOH-700 and C-700 samples were also examined in a two cell system, and the results are shown in Fig. 6. The CV curves in rectangular-like shapes indicate a good capacitive behavior over a wide range of voltage (from 0 to 1 V, see Fig. 6a). The electrochemical performance of C/KOH-700 is much better than that of C-700. The galvanostatic charge/discharge curves shown in Fig. 6b agree with the CV curves. Fig. 6c is the EIS of C/KOH-700 and C-700 samples. C/KOH-700 has a less diameter of the semicircle than that of C-700, clarifying the importance of the hierarchical porous structure for ion diffusion when both possess the similar nitrogen content. Based on the total mass of the two electrodes, the specific capacitance of C-700 maintains 125 F g^{-1} at 0.05 A g^{-1}. In contrast, good capacitance retention is observed in the C/KOH-700 supercapacitor. Its specific capacitance reaches 239 and 201 F g^{-1} at 0.05 and 1.0 A g^{-1}, respectively, which is nearly 2-fold higher than that of C-700. Fig. 6e shows the Ragone plots of both samples and their energy and power characteristics. C/KOH-700 and C-700 show the specific energy of 8.3 and 2.7 W h kg^{-1}, corresponding to the specific power of 1105 and 907 W kg^{-1}, respectively. The increased power characteristics of C/KOH-700 originate from its hierarchical pore structure as shown in Fig. 3. Additionally, good electrochemical property and wettability contribute to the efficient electron/ion transfer and the large exposure of active sites, respectively.
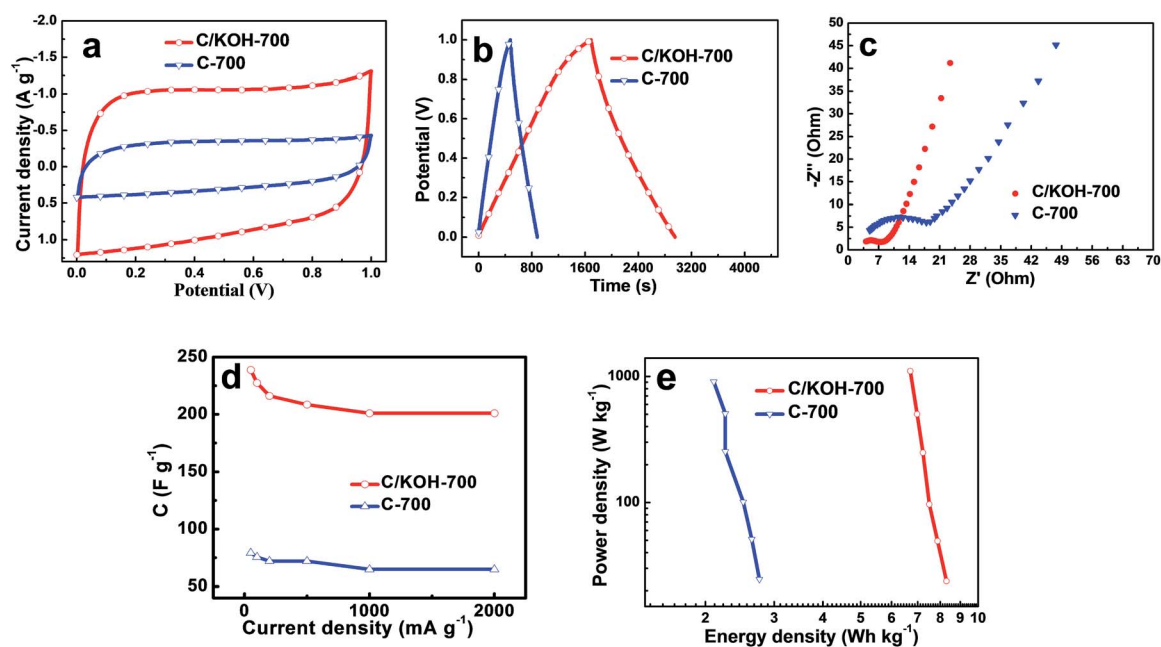

Fig. 6 Electrochemical performances of C/KOH-700 and C-700 samples measured in a two-electrode system in a 6 M KOH electrolyte: (a) CV plots at the scan rate of 20 mV s^{-1}; (b) charge–discharge curves at the current density of 50 mA g^{-1}; (c) Nyquist plots; (d) specific capacitances at different current densities; (e) Ragone plots.

Conclusions

Nitrogen-decorated HPCs were successfully prepared from shrimp shell by the self-templating method combined with KOH activation. This method for the fabrication of a hierarchical porous structure is very simple, efficient and sustainable. The intrinsic $CaCO_3$ in shrimp shell plays the self-template role usually needed in the template method, and thus simplifies the preparation process of HPCs. Shrimp shell as a kind of natural biomass waste in millions of tons, is a potential "zero-cost" carbon precursor, which offers a "green material" to produce HPCs. Simultaneously, this strategy provides a green and high value application of seafood waste. Additionally, the obtained nitrogen-decorated porous carbon shows good electrochemical performance as an EC electrode, which exhibits good capacitive behavior including large capacitance, long cycle life, and high energy and power densities. The prepared HPCs also have good application future in many fields such as electrochemistry, catalysis and gas storage.

Acknowledgements

References

1 Y. Zhai, Y. Dou, D. Zhao, P. F. Fulvio, R. T. Mayes and S. Dai, *Adv. Mater.*, 2011, **23**, 4828–4850.

2 M. Inagaki, H. Konno and O. Tanaike, *J. Power Sources*, 2010, **195**, 7880–7903.

3 P. Simon and Y. Gogotsi, *Nat. Mater.*, 2008, **7**, 845–854.

4 Y. S. Yun, S. Y. Cho, J. Shim, B. H. Kim, S. J. Chang, S. J. Baek, Y. S. Huh, Y. Tak, Y. W. Park, S. Park and H. J. Jin, *Adv. Mater.*, 2013, **25**, 1993–1998.

5 A. Jain, C. Xu, S. Jayaraman, R. Balasubramanian, J. Y. Lee and M. P. Srinivasan, *Microporous Mesoporous Mater.*, 2015, **218**, 55–61.

6 Y. Zhao, M. Liu, L. Gan, X. Ma, D. Zhu, Z. Xu and L. Chen, *Energy Fuels*, 2014, **28**, 1561–1568.

7 Y. Zhao, M. Liu, X. Deng, L. Miao, P. K. Tripathi, X. Ma, D. Zhu, Z. Xu, Z. Hao and L. Gan, *Electrochim. Acta*, 2015, **153**, 448–455.

8 M. Liu, J. Qian, Y. Zhao, D. Zhu, L. Gan and L. Chen, *J. Mater. Chem. A*, 2015, **3**, 11517–11526.

9 K. Xia, Q. Gao, J. Jiang and J. Hu, *Carbon*, 2008, **46**, 1718–1726.

10 Y. S. Hu, P. Adelhelm, B. M. Smarsly, S. Hore, M. Antonietti and J. Maier, *Adv. Funct. Mater.*, 2007, **17**, 1873–1878.

11 S. J. Yang, T. Kim, J. H. Im, Y. S. Kim, K. Lee, H. Jung and C. R. Park, *Chem. Mater.*, 2012, **24**, 464–470.

12 G. Xu, B. Ding, L. Shen, P. Nie, J. Han and X. Zhang, *J. Mater. Chem. A*, 2013, **1**, 4490–4496.

13 D. Liu, P. Yuan, D. Tan, H. Liu, M. Fan, A. Yuan, J. Zhu and H. He, *Langmuir*, 2010, **26**, 18624–18627.

14 W. Xia, B. Qiu, D. Xia and R. Zou, *Sci. Rep.*, 2013, **3**, 1–7.

15 L. Wan, J. Wang, L. Xie, Y. Sun and K. Li, *ACS Appl. Mater. Interfaces*, 2014, **6**, 15583–15596.

16 T. C. Chou, C. H. Huang, R. A. Doong and C. C. Hu, *J. Mater. Chem. A*, 2013, **1**, 2886–2895.

17 Y. Wang, S. Tao and Y. An, *Microporous Mesoporous Mater.*, 2012, **163**, 249–258.

18 P. Cheng, S. Gao, P. Zang, X. Yang, Y. Bai, H. Xu, Z. Liu and Z. Lei, *Carbon*, 2015, **93**, 315–324.

19 F. Xu, Z. Tang, S. Huang, L. Chen, Y. Liang, W. Mai, H. Zhong, R. Fu and D. Wu, *Nat. Commun.*, 2015, **6**, 7221.

20 D. Wu, Z. Li, M. Zhong, T. Kowalewski and K. Matyjaszewski, *Angew. Chem., Int. Ed.*, 2014, **53**, 3957–3960.

21 Y. Liang, H. Liu, Z. Li, R. Fu and D. Wu, *J. Mater. Chem. A*, 2013, **1**, 15207–15211.

22 M. Zhong, E. K. Kim, J. P. McGann, S. E. Chun, J. F. Whitacre, M. Jaroniec, K. Matyjaszewski and T. Kowalewski, *J. Am. Chem. Soc.*, 2012, **134**, 14846–14857.

23 Y. Deng, Y. Xie, K. Zou and X. Ji, *J. Mater. Chem. A*, 2016, **4**, 1144–1173.

24 R. J. White, M. Antonietti and M. M. Titirici, *J. Mater. Chem.*, 2009, **19**, 8645–8650.

25 J. Romanos, M. Beckner, T. Rash, L. Firlej, B. Kuchta, P. Yu, G. Suppes, C. Wexler and P. Pfeifer, *Nanotechnology*, 2012, **23**, 1–7.

26 X. Y. Chen, C. Chen, Z. J. Zhang, D. H. Xie, X. Deng and J. W. Liu, *J. Power Sources*, 2013, **230**, 50–58.

27 D. H. Jurcakova, M. Seredych, G. Q. Lu and T. J. Bandosz, *Adv. Funct. Mater.*, 2009, **19**, 438–447.

28 Y. S. Yun, M. H. Park, S. J. Hong, M. E. Lee, Y. W. Park and H. J. Jin, *ACS Appl. Mater. Interfaces*, 2015, **7**, 3684–3690.

29 P. K. Tripathi, M. Liu, Y. Zhao, X. Ma, L. Gan, O. Noonan and C. Yu, *J. Mater. Chem. A*, 2014, **2**, 8534–8544.

30 X. Sheng, N. Daems, B. Geboes, M. Kurttepeli, S. Bals, T. Breugelmans, A. Hubin, I. F. J. Vankelecom and P. P. Pescarmona, *Appl. Catal., B.*, 2015, **176–177**, 212–224.

31 J. L. Shi, C. Tang, H. J. Peng, L. Zhu, X. B. Cheng, J. Q. Huang, W. Zhu and Q. Zhang, *Small*, 2015, **11**, 5243–5252.

32 W. Ding, Z. D. Wei, S. G. Chen, X. Q. Qi, T. Yang, J. S. Hu, D. Wang, L. J. Wan, S. F. Alvi and L. Li, *Angew. Chem., Int. Ed.*, 2013, **52**, 11755–11759.

33 J. Y. Qu, C. Geng, S. Y. Lv, G. H. Shao, S. Y. Ma and M. B. Wu, *Electrochim. Acta*, 2015, **176**, 982–988.

34 H. Zhu, J. Yin, X. Wang, H. Wang and X. Yang, *Adv. Funct. Mater.*, 2013, **23**, 1305–1312.

35 J. Y. Qu, F. Gao, Q. Zhou, Z. Y. Wang, H. Hu, B. B. Li, W. B. Wan, X. Z. Wang and J. S. Qiu, *Nanoscale*, 2013, **5**, 2999–3005.

36 L. Zhao, L. Z. Fan, M. Q. Zhou, H. Guan, S. Qiao, M. Antonietti and M. M. Titirici, *Adv. Mater.*, 2010, **22**, 5202–5206.

37 J. Li, Z. Ren, Y. Zhou, X. Wu, X. Xu, M. Qi, W. Li, J. Bai and L. Wang, *Carbon*, 2013, **62**, 330–336.

38 F. Su, C. K. Poh, J. S. Chen, G. Xu, D. Wang, Q. Li, J. Lin and X. W. Lou, *Energy Environ. Sci.*, 2011, **4**, 717–724.

39 M. Wu, P. Ai, M. Tan, B. Jiang, Y. Li, J. Zheng, W. Wu, Z. Li, Q. Zhang and X. He, *Chem. Eng. J.*, 2014, **245**, 166–172.

40 M. Wu, Q. Zha, J. Qiu, Y. Guo and H. Shang, *Carbon*, 2004, **42**(1), 195–200.

41 Y. M. Chen, Z. Li and X. W. Lou, *Angew. Chem., Int. Ed.*, 2015, **54**, 10521–10524.

42 Z. Lei, L. Lu and X. S. Zhao, *Energy Environ. Sci.*, 2012, **5**, 6391–6399.